Applied Materials Today 24 (2021) 101135

Contents lists available at ScienceDirect

Applied Materials Today

journal homepage: www.elsevier.com/locate/apmt

# Corrosion mechanisms of magnetic microrobotic platforms in protein media

Ehsan Rahimi[a], Ruben Offoiach[a], Siyu Deng[b], Xiangzhong Chen[b], Salvador Pané[b,*], Lorenzo Fedrizzi[a], Maria Lekka[a,c,*]

[a] Polytechnic Department of Engineering and Architecture, University of Udine, 33100 Udine, Italy
[b] Multi-Scale Robotics Lab (MSRL), Institute of Robotics & Intelligent Systems (IRIS), ETH Zurich, Zurich 8092, Switzerland
[c] CIDETEC, Basque Research and Technology Alliance (BRTA), Po. Miramón 196, 20014 Donostia-San Sebastián, Spain

ARTICLE INFO

*Article history:*
Received 2 May 2021
Revised 26 July 2021
Accepted 27 July 2021

*Keywords:*
Corrosion mechanism
Magnetic micro-robots
Simulated body fluids
Biodegradation
Albumin protein

ABSTRACT

The field of biomedical small-scale swimmers has made major progress during the last two decades. While their locomotion aspects and functionalities have been demonstrated, there are key aspects that have been often overlooked such as their service live durability, which difficult their translation to the clinics. Several swimmers consist of combinations of metals and alloys that, while they excel in their functionalities, they fail in their stability due to corrosion in highly aggressive complex body fluids. Here, for the first time the corrosion mechanism of a widely employed design in magnetic microrobots, a gold-coated magnetic NiCo alloy, is assessed. A systematic approach by combining electrochemical and surface analysis techniques is reported, which shed light on the degradation mechanisms of these systems in simulated body fluids. While results demonstrate that Au coatings remarkably enhance the surface nobility and resistance to corrosion/biodegradation of NiCo in an aggressive environment containing albumin protein, Au coatings' intrinsic defects lead to a galvanic coupling with the NiCo substrate. The coordination of protein with NiCo further accelerates corrosion causing morphological changes to the swimmers' surface. Yet, the formation of a phosphate-based layer acts as a barrier to the metal release after long immersion periods.



## 1. Introduction

Small-scale swimmers, which comprise motors and robots, are tiny machines capable of moving and operating at the micro- and nano realms. These motile micro- and nanodevices have been proposed for a large variety of applications including manufacturing, material removal, environmental remediation, targeted drug delivery, nanosurgery, and isolation of biological targets [1-4].

The controlled locomotion of small-scale swimmers in liquid environments has been the object of study for at least two decades, as motion at low Reynolds numbers requires the execution of non-reciprocal motions for achieving translational displacement (at least for Newtonian fluids) [5]. To this end, researchers have investigated several strategies to provide the energy necessary for the motion of micro- and nanostructures [6, 7]. Efforts have been made to develop tiny machines that can display one or more locomotion mechanisms including tumbling, rolling, corkscrewing, crawling, shuttling, and contraction [8]. Two main approaches exist for providing a driving force necessary for the motion of small-scale swimmers. In the first, the micro- or nanostructure acts as a platform for triggering a chemical or an electrochemical reaction, which results in the propulsion of the structure. These reactions take place on the swimmer's surface, which serves as a reactant or as a catalyst for the transformation of the chemical species present in the surrounding media [9, 10]. In this situation, swimmers are motors (not robots) because their directionality and speed cannot be controlled. The second approach consists of using small-scale structures that are responsive to an external source of energy, such as magnetic or electric fields, ultrasound, light or combinations of these, which causes the structure to move [7, 11]. The swimmers that are controlled by external sources of energy are known as robots, because their speed and directionality can be externally controlled by tuning the energy of the source. In both approaches, not only the components but also their geometry are key for their optimal motion or manipulation [12]. However,

* Corresponding authors.
*E-mail addresses:* rahimi.ehsan@spes.uniud.it (E. Rahimi), ruben.offoiach@uniud.it (R. Offoiach), sdeng@ethz.ch (S. Deng), chenxian@ethz.ch (X. Chen), vidalp@ethz.ch (S. Pané), lorenzo.fedrizzi@uniud.it (L. Fedrizzi), mlekka@cidetec.es (M. Lekka).

https://doi.org/10.1016/j.apmt.2021.101135

as swimmers are ultimately designed for the realization of tasks, it might be necessary to incorporate additional components in the final swimmer architecture [3].

Arguably, the use of external magnetic fields is one of the most versatile approaches for the manipulation of magnetic micro- and nanorobots, as a wide variety of swimming mechanisms can be achieved by changing the way magnetic fields are applied (i.e. rotating, oscillating, gradients or combinations thereof) [13]. Additionally, considering that some of the most sought applications are in the biomedical area, magnetic fields are suitable for biomedical purposes owing to their high biocompatibility characteristics towards biological tissues [13, 14]. Most magnetic micro- and nanorobots are fabricated of ferro- and ferrimagnetic metals, alloys or ceramic oxides containing at least one of the following elements: Fe, Ni, and Co [13, 15, 16]. Note that the manipulation of diamagnetic and paramagnetic small-scale robots has also been investigated, but examples are few in comparison to ferro- and ferrimagnetic devices. Magnetic micro- and nanorobots can be produced using different techniques such as physical vapour deposition (PVD), three-dimensional direct laser writing (TDLW), assembly of materials, and template-assisted electrodeposition [12]. The latest has attracted many researchers as it is a low-cost method that does not require special equipment and allows the formation of several micro- and nanoarchitectures made of different materials ranging from metals to polymers [12, 17-19].

In terms of motion and processability, ferromagnetic metals and alloys are very attractive for the construction of magnetic micro- and nanorobots [20]. Additionally, these materials exhibit optimal properties for magnetic manipulation, such as high saturation magnetization and high magnetic susceptibility. Furthermore, their magnetic softness/hardness can be modulated by tailoring their crystal structure and/or by alloying with other magnetic and non-magnetic elements [21]. Unfortunately, most ferromagnetic metals and alloys degrade, especially when they are in contact with fluids, which can result in the release of toxic ions into the surrounding media [22, 23]. amongst the three ferromagnetic elements of the periodic table, Fe is the only one that displays biocompatible characteristics as most of the surrounding tissues can uptake iron ions via transferrin [24]. While iron is highly prone to degrade and can be remediated by the body, iron can also be cytotoxic to certain cells, such as the retinal tissue [25]. Other alloys, such as NiCo, present a good corrosion resistance in different environments thanks to their ability to create a stable passive film. However, media such as biological fluids can result in their slow degradation and the release of metal ions, which can accumulate in cells and tissues and ultimately affect the human immune system [26]. Finally, degradation of ferromagnetic materials also implies a deterioration of their magnetic and mechanical properties, which can severely impair their swimming performance, speed, and controllability.

Considering all these facts, magnetic small-scale robots can be designed as fully degradable, or composed of an inert part that prevents any deleterious effect to the performance of the device or to the surrounding environment. If designed in a degradable form, swimmers must contain metals that exhibit biocompatibility characteristics (i.e. non-toxic, non-carcinogenic, non-allergenic, and non-inflammatory) [27, 28]. Additionally, the biodegradability should be programmed so that swimmers have a sufficient lifetime to perform the tasks for which they are designed [29]. Combinations of magnetic iron or iron-based alloys containing elements such as Zn, Mn, or additional layers containing these elements, are suitable candidates for biodegradable swimmers. If swimmers are composed of magnetic parts containing toxic elements (i.e.: Ni, Co), protective films against their degradation in the specific working environment should be incorporated. Inert metals, such as Au, Pt, Ag or metals exhibiting a passive behavior like Ti, are appropriate for building non-degradable magnetic swimmers. Surface protection can improve the biocompatibility characteristics of magnetic swimmers and limit the release of toxic ions from magnetic components [9, 18]. For example, noble metals or oxides with insulating properties are a widely adopted option for preventing the metal ion release process [30, 31]. However, from the corrosion point of view, the small dimensions of micro- and nanorobotic architectures and the complexity of the human body environment (interaction with proteins, cells, and tissues) should be carefully considered [32-34]. The presence of micro- or nanoscale defects in protective coatings, which could be considered negligible in large scale components, can become dramatically relevant at the micro- and nanoscale dimensions. Specially, the galvanic coupling of metals with a marked difference in nobility can become significantly exacerbated in small-scale swimmers composed of different metal segments, or on those metallic designs coaxially coated by other metals or alloys [33, 35].

Corrosion can have a dramatic impact on small-scale swimmers. To date there are only a few works that have addressed the corrosion phenomena on micro- or nano-devices [30, 33, 34]. However, corrosion has been studied with indirect methods, such as morphological analyses, to observe the degradation after a certain period of immersion in the corrosive fluid [30, 34], chemical analyses of the corrosive media to measure ions release [33, 34], or through the deterioration of the performances [30].

In this work, we give an insight into the degradation mechanisms of magnetic microrobots consisting of NiCo micropillars (NiCo-MPs), both uncoated and Au-coated, in simulated human body fluids, using both electrochemical and surface analysis techniques for the first time. NiCo alloys have been widely used for small-scale robotic designs due to their superior mechanical properties as well as their optimal soft magnetic features. However, the degradation mechanisms of NiCo alloys in protein-containing biological fluids has not been thoroughly investigated [36], as these alloys are not commonly used as implants. Yet, both Ni and Co are common elements in most of the widely used metallic biomaterials, such as AISI 316 stainless steel and CoCrMo alloys. Different studies have evaluated the corrosion resistance of these alloys as well as of Ti6Al4V in a variety of simulating body fluids [37], such as 0.9% NaCl, phosphate buffer solution (PBS), Hanks' and Ringer's solutions. Phosphate species ($H_2PO_4^-$/$HPO_4^{2-}$) in physiological body fluids play a critical role in the corrosion resistance behavior of implanted metallic biomaterials due to the formation of a phosphate thin film on the material surface [38]. A recent study comparing the effect of different solutions on the protein absorption on Ti6Al4V [39] indicated that the phosphate film formed in PBS solution is thicker in comparison to that formed in Hanks' solution.

The effect of proteins such as bovine serum albumin (BSA), human serum albumin (HSA) on the degradation of different passive metals such as CoCrMo [40-42], Ti6Al4V [39, 43-45] and AISI 316 L SS [46-48] has also been investigated. The impact of protein on the corrosion of passive alloys and the metal ions release in body fluids is determining [49]. For instance, it has been reported that the albumin protein can accelerate the anodic dissolution and suppress the cathodic reactions of SS 316 L (Low carbon) 0.9% NaCl solution [48]. Another study reports that the presence of BSA or lysozyme in PBS solution increases the Fe, Cr, Ni and Mn release from stainless steels (AISI 304, 310 and 316 L) reducing their corrosion resistance [47]. The same effect has been reported for CoCrMo alloy, where the presence of BSA in PBS solution affects the passivation kinetics hindering the formation of a passive film (when the alloy is anodically polarized) during long passivation times [40]. SKPFM studies on Ti6Al4V alloy in different body fluid simulating solutions in presence of BSA, demonstrated that the BSA molecules compete with the phosphate species to the formation of an ab-

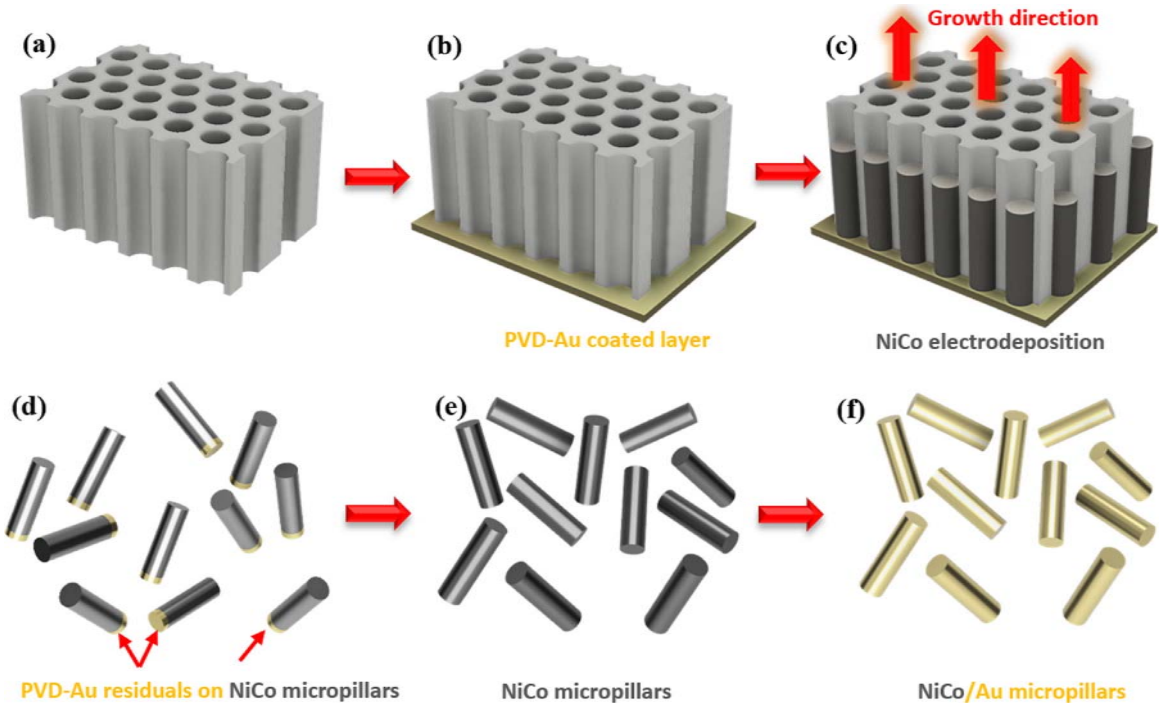


**Fig. 1.** A schematic representation of the NiCo and NiCo/Au-MP fabrication process, (a) organic membrane template (MT) with 1 $\mu$m pore diameter and 100 $\mu$m length, (b) Physical vapour deposition of Au on one side of the MT, (c) NiCo electrodeposition within the pores, (d) Detachment of the formed NiCo-MP by dissolving the MT, (e) Dissolving of the PVD Au coated layer, (f) Au thin layer coated on NiCo-MP by electroless deposition.

sorbed film on the passive film accelerating the degradation processes [39, 45]. Similar effects could be expected on NiCo alloys. Because of their potential cytotoxicity, small-scale robots made of these alloys are usually coated with Au.

However, the presence of defects on small-scale structures can accelerate their corrosion by galvanic coupling. To understand the role of defects in the degradation of microscale structures, the corrosion resistance and corrosion mechanisms, both uncoated and Au-coated magnetic microstructures were tested after short and long-time immersion in phosphate-buffered saline (PBS) solution with and without the addition of bovine serum albumin (BSA) protein. A combination of large-scale electrochemical techniques, field-emission scanning electron microscopy (FE-SEM), atomic force microscopy (AFM), and scanning Kelvin probe force microscopy (SKPFM), were used to understand the degradation of the swimmers. The long-term degradation was also evaluated through inductively coupled plasma-atomic emission spectrometry (ICP-AES) analyses of the media, where the MPs were immersed for varying periods of time. Our findings do not only apply to micro- or nanoswimmers, but also to other small-scale metal architectures.

## 2. Experimental procedure

### 2.1. NiCo and NiCo/Au micropillar fabrication

The fabrication steps for the production of NiCo and NiCo/Au-MPs are reported in Fig. 1. The technique is based on template-assisted electrodeposition using commercially available membranes (PVP-Free Nuclepore Hydrophobic Membrane from Whatman, with a pore size of 1 $\mu$m and pore length of 10 $\mu$m). A thin layer of Au (~100 nm) was deposited on the membrane by PVD. This thin conductive layer acted as a cathode for the nucleation and growth of NiCo pillars. The electrodeposition process was performed with the three-electrode cell using an Autolab potentiostat (Metrohm, PGSTAT204). The Au coated membrane template, a Pt plate, and an $Ag/AgCl/Na_2SO_4$ electrode were arranged as cathode, anode, and the reference electrode, respectively. The chemical composition and parameters of the Ni-Co electrolyte are reported in Table S1. To obtain the NiCo-MPs, a potentiostatic polarization was applied at −1.1 V vs. $Ag/AgCl/Na_2SO_4$ for approximately 150 s. The membrane was then dissolved by immersion in Chloroform (Sigma–Aldrich) for 1 hour to obtain the separated NiCo-MPs. The sputtered Au layer was removed by etching in Gold etchant, nickel compatible (Sigma- Aldrich). Finally, the NiCo-MPs were cleaned in an ultrasound bath in acetone, ethanol, and de-ionized (DI) water. To improve the biocompatibility characteristics and prevent the metal ions release, a thin layer of Au was deposited on the NiCo-MPs using an immersion Au commercial bath (TRANSENE INC). The deposition was carried out at 90 °C for 20 min, maintaining the NiCo-MPs in suspension by stirring. Consequently, the NiCo/Au-MPs were cleaned by ultrasonication in acetone for 20 min and rinsed with DI water several times.

### 2.2. Microscopy characterizations

The MPs have been characterized using FE-SEM, AFM, and SKPFM techniques. For the analysis, both NiCo and NiCo/Au-MPs were mixed with ethanol and then spread onto a glassy carbon plate (C000502, Goodfellow). The microstructure and the chemical composition of the MPs both prior to and after immersion in the corrosive environment was evaluated using an FE-SEM (JEOL, JSM-7610FPlus) equipped with an energy dispersive X-ray spectroscopy (EDXS, OXFORD X-MAX 20) analysis system. AFM and SKPFM mappings were obtained to evaluate the topography and surface Volta potential differences of NiCo and NiCo/Au-MPs. The scanning probe microscope (SPM) was a Digital Instruments Nanoscope IIIa Multimode with an n-type doped silicon pyramid single crystal tip coated with PtIr5 (SCM-Pit probe). The surface Volta potential mappings were carried out using the dual-scan mode. In the first scan, topography data was obtained using the tapping mode, and the second scan surface Volta potential was captured by lifting the

tip up to 100 nm. Topography and Volta potential mappings were obtained in air at 25 C° with an approximate relative humidity of 28%, a pixel resolution of 512 × 512, a zero-bias voltage, and a scan frequency rate of 0.2 Hz.

### 2.3. Electrochemical measurements

#### 2.3.1. Samples preparation

In order to obtain a suitable working electrode for the electrochemical measurements, 2 × 2cm$^2$ indium tin oxide coated glass (ITO,18–20 ohms/sq, techinstro) was coated with a conductive polymer (Nafion® 117, Sigma–Aldrich) in which the MPs had been previously dispersed. Nafion® was used to ensure the electrical connection between the MPs and the ITO glass [50-52]. Nafion® as a perfluorinated anionic polyelectrolyte has been extensively used in recent years for the fabrication of redox polymer-modified electrodes with high chemical stability and good biocompatibility, particularly for the detection of protein adsorption [53, 54]. The procedure was optimized to achieve samples where part of the pillars are not fully embedded in Nafion®, ensuring enough exposed metallic area to the electrolyte. Several attempts were made to achieve this aim, and the obtained specimens were controlled by FE-SEM. The optimized preparation procedure is as follows: first, 40 mg of either NiCo or NiCo/Au-MPs were gently mixed with 150$\mu$L of ethanol and 20$\mu$L of Nafion® (as also reported in other studies [55, 56]). The obtained solution was uniformly spread on the ITO glass by a spin coater (Ossila, UK) using a spin speed of 500 rpm for 20 s. Under these conditions, only the first layer of MPs was embedded fully in Nafion®, while the top layer was composed of partially embedded MPs leaving part of their surface in direct contact with the electrolyte during the electrochemical measurements as shown in Figure S1. Finally, the MPs coated ITO glass was dried at 60 C° for 1 hour in the air-oven. An optical microscope and image analysis method (ImageJ software [57]) was used to estimate the percentage of the ITO glass surface occupied by MPs during exposure in the solution for all electrodes, as shown in Figure S2.

#### 2.3.2. Electrolyte composition and electrochemical measurements procedures

PBS solution was used as a base electrolyte to perform all electrochemical measurements. 1 g/L of BSA protein (lyophilized powder, ≥96% agarose gel electrophoresis, Sigma–Aldrich) was added to the PBS solution to obtain conditions closer to those of the human body to evaluate its influence on the MPs degradation. The chemical composition of the electrolyte is given in Table S2 [39]. All electrochemical measurements were performed at 25C° and pH 7.4 ± 1 using an AUTOLAB PGSTAT 30 potentiostat in a three electrodes conventional cell. The coated ITO glass was used as a working electrode, an Ag/AgCl/KCl$_{3M}$ electrode (+222 vs. SHE) as a reference, and a Pt wire as the counter electrode. The potentiodynamic polarization (PDP) measurements were carried out at a scan rate of 1 mV.s$^{-1}$ from cathodic (- 200 mV vs. open circuit potential (OCP)) to anodic potentials up to 1200 mV vs. Ag/AgCl/KCl$_{3M}$, if no breakdown was observed earlier. PDP measurements were done after 1-hour immersion in the electrolyte to stabilize the OCP. The long-term degradation of NiCo and NiCo/Au-MPs was investigated by OCP and electrochemical impedance spectroscopy (EIS) measurements in both PBS and PBS+1 g.L − 1 BSA environments for 30 days and the following "control-times": 1 h, 2 h, 4 h, 8 h, 12 h, 1day, 2days, 4days, 8days, 18days, and 30days. EIS measurements were performed in a frequency range of 10 mHz to 10 kHz by applying a sinusoidal excitation signal of ±10 mV vs. OCP.

### 2.4. Long-time free immersion tests

NiCo and NiCo/Au-MPs (not supported onto ITO glass) were also immersed in PBS and PBS+BSA environments at pH 7.4 and 25 °C for a period of up to 140 days. The solutions were appropriately prepared after 7, 56, and 140 days and analysed by measuring the pH and using ICP-AES (Agilent 5800) to determine the released Ni and Co ions. The calibration was done using an ICP-standard 23 elements solution in 5% nitric acid (Merck solution IV). Before ICP-AES analysis, the whole PBS and PBS+BSA solutions containing released Ni and Co ions were digested in acidic media [58]. The ICP-AES analyses were performed at ppm (mg/L) concentration for all solutions. The MPs were collected, cleaned in ethanol and DI water with ultrasound, and analysed by FE-SEM and SKPFM to control the morphology, the extent of the corrosion attack, and surface Volta potential evaluations. The magnetic response of NiCo-MPs before and after 140 days immersion in different media was conducted by placing a swarm of MPs in a beaker, and applying an external magnetic field using a stack of permanent magnets.

## 3. Results and discussion

### 3.1. Microstructure and electronic properties of NiCo and NiCo/Au-MPss

SEM micrographs of a NiCo and NiCo/Au single micropillar, together with elementary EDXS maps, are reported in Fig. 2a and b, while lower magnification micrographs showing different MPs are reported in Figure S3. The surface of NiCo-MPs was very smooth (Fig. 2a), and the elementary EDXS maps reveal a uniform distribution of Ni and Co. The semi-quantitative EDXS analyses demonstrate that the pillars are composed of 78% Ni and 22% Co (at%). The presence of O reveals that the surface of the pillar is covered by the native passive film (NiO and CoO oxides [59]). NiCo/Au-MPs present a rougher surface and the elementary EDXS maps shows that the O signal differences disappear (no contrast between the MPs and the glassy carbon plate), while Ni and Co can still be detected as the thickness of the Au layer is very low.

From a closer look at the top surface of NiCo-MP in Fig. 3a, we can discern some nano-pores and nano-defects mainly due to hydrogen evolution during the deposition and to the intrinsic roughness of the membrane walls. The surface roughness of the NiCo-MPs, measured by AFM, is about 10–30 nm. The high magnification image of NiCo/Au-MP in Fig. 3b shows that the Au coating presents a cauliflower morphology. However, the Au layer does not uniformly cover all the observed micropillars. Uncovered regions, micro, and nano-sized defects are present, as indicated in Fig. 3c–e. We can distinguish two main types: areas where part of the coating has been detached (Fig. 3c and e), perhaps during the post-deposition and/or cleaning procedure, and uncovered areas (Fig. 3d) where the deposit has not grown over the NiCo substrate. In both cases, the NiCo substrate is in direct contact with the environment. These types of defects are very common on low thickness immersion deposits and are linked to the deposition process. Such defects are negligible over large-scale objects but in the case of the micro-sized pillars, these defects can significantly accelerate the metal ions' release from the substrate due to galvanic coupling (vide infra). AFM topographic images of NiCo and NiCo/Au-MPs are shown in Fig. 4a and b, respectively, together with the height line profiles (Fig. 4c). The NiCo/Au-MPs has slightly increased height and diameter values than the NiCo-MP. Based on the difference in height measured by AFM (about 0.18 $\mu$m on measurements made by FE-SEM in the places where the Au coating has been detached (Fig. 3c)), the thickness of the Au layer can be estimated at about 90–100 nm.

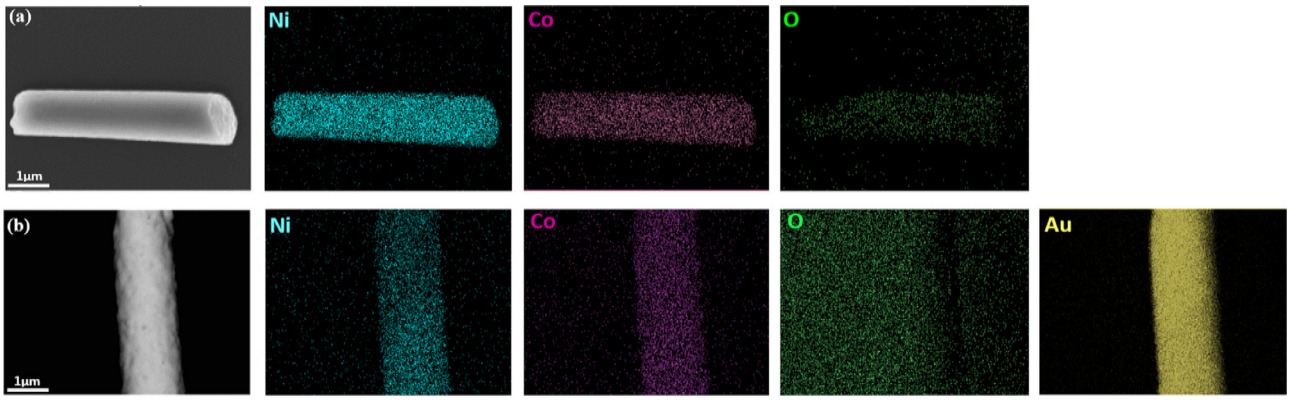


**Fig. 2.** SEM and EDXS elemental maps of (a) NiCo and (b) NiCo/Au-MPs.

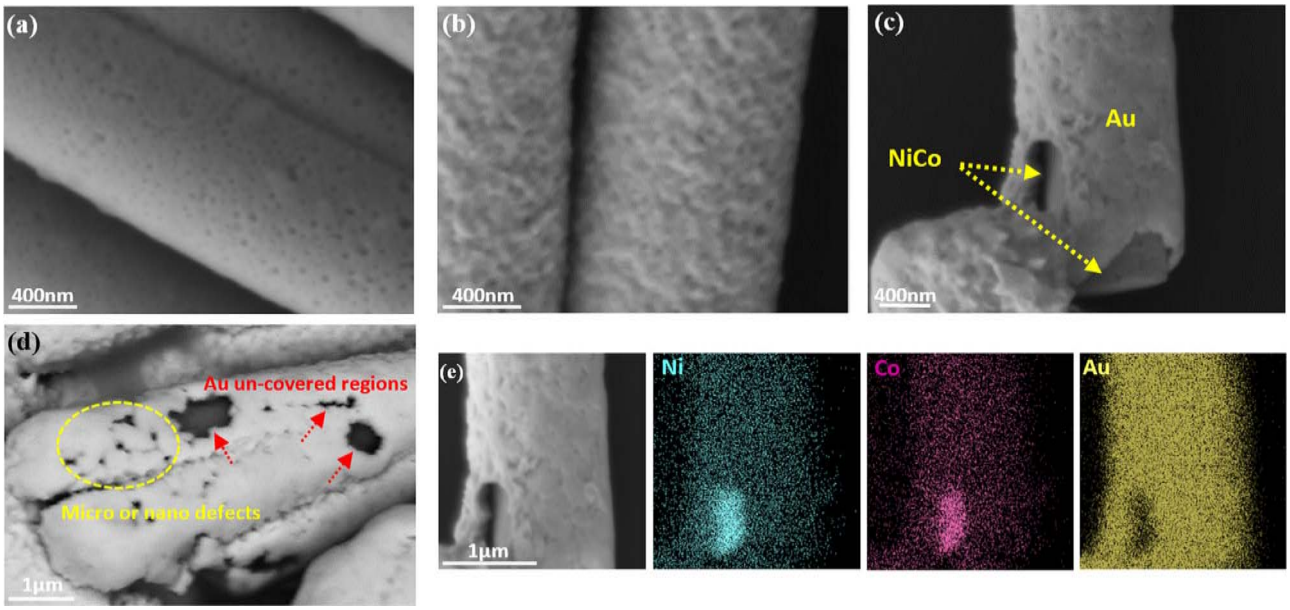


**Fig. 3.** High magnification images of (a) NiCo and (b, c, d) NiCo/Au-MPs, (e) SEM micrograph and EDXS elemental maps of an NiCo/Au-MP, which exhibits the presence of an NiCo/Au un-covered interface.

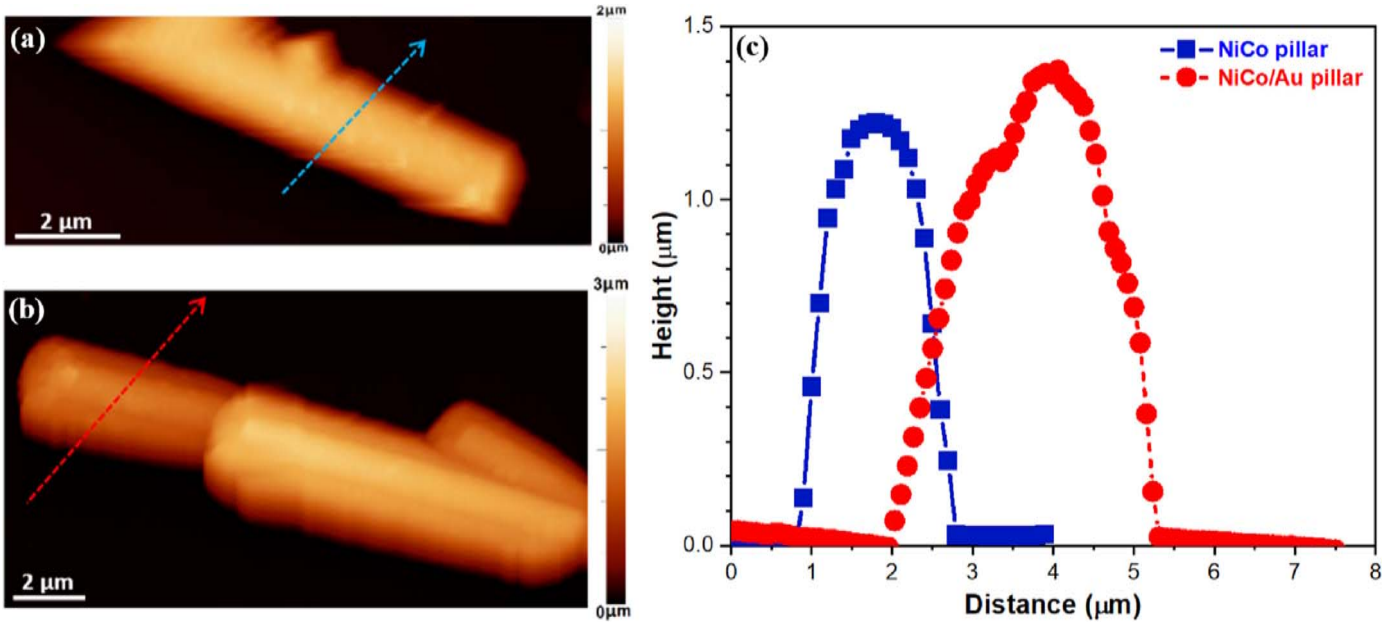


**Fig. 4.** Topography images of (a) NiCo and (b) NiCo/Au-MPs on glassy carbon, (c) Topography line profiles of both NiCo and NiCo/Au-MPs.

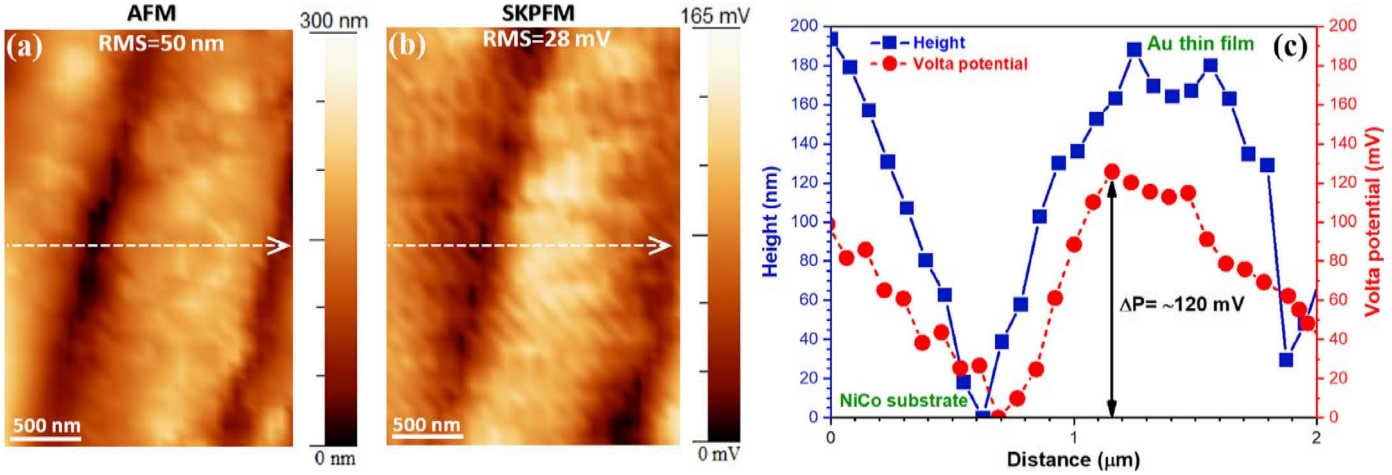


**Fig. 5.** (a) Topography and (b) surface Volta potential images of NiCo/Au-MP with small porosities, (c) Topography and surface Volta potential line profiles from (a and b).

In order to verify if the defects present on the Au layer can accelerate the NiCo dissolution due to galvanic coupling, surface Volta potential maps were obtained on areas presenting defects. Indeed, the differences in the surface electronic properties of materials can be used as a criterion to determine the surface conductivity, which plays a significant role on the electrochemical interactions [60, 61]. According to previous studies [62-64], materials with high surface Volta potential or work function energy (WFE) values present higher stability of valance electrons or a more stable electronic state, inhibiting valence electrons from participating in electrochemical reactions. Consequently, materials with higher surface Volta potential behave with higher electrochemical nobility [65-67]. High magnification topographic and Volta potential maps of a NiCo/Au-MP on a defected zone as the one indicated by the yellow circle in Fig. 3d are reported in Fig. 5a and b, respectively, together with the corresponding line profiles in Fig. 5c. Comparing the topographic and the Volta potential maps, it is clear that in the areas with low height, the NiCo is uncovered (lower Volta potential). The potential difference between the Au coating and the uncovered NiCo substrate is approximately 120 mV (Fig. 5c). As this difference appears quite high considering the passive layer of NiCo, the same measurements were also performed on large scale specimens produced by partially covering with an Au thin layer electroformed NiCo alloy with the same composition as the NiCo-MP. The results are presented in Figure S4. The measured Volta potential difference in this case was about 150 mV, confirming the results obtained on the MP surface. It is hence fair to predict a marked galvanic coupling between the Au coating and the NiCo substrate with a localization of the cathodic reactions on the Au and the anodic reactions on the NiCo.

### *3.2. Electrochemical study of NiCo and NiCo/Au-MPs in PBS with and without BSA*

Fig. 6a shows the OCP curves of NiCo and NiCo/Au-MP samples immersed in the PBS solution with and without 1 $g.L^{-1}$ BSA protein for 1 hour at 25 °C in aerated conditions, together with the curves corresponding to ITO glass and ITO glass+Nafion® samples immersed in PBS and used as references. The OCP curves of all samples showed a relatively fast stabilization. The measurements performed in PBS electrolyte showed that the deposition of a Nafion® layer onto the ITO glass leads to a marked ennoblement of the potential (~390 mV vs. Ag/AgCl against −68 mV vs. Ag/AgCl of the bare ITO glass). This is due to the hydrophobic behavior of Nafion®, which acts as a barrier to diffuse the oxygen, water molecules, and other ions to the conductive surface of ITO glass [68].

Instead, the dispersion of both MPs types in the conductive polymer led to a decrease in the OCP, and was more evident in the samples prepared with NiCo-MPs. It should also be noted that, due to the nature of the analysed specimens, the measured potential is always a mixed potential of all the components of the specimens. Considering the preparation procedure, we can assume that the same content of MPs is present on the specimens' surface in all cases, and thus a comparison between the different types of MPs can be done quite safely. The deposition of an Au layer on the NiCo-MPs led, as anticipated, to an increase of the OCP of about 105 mV vs. Ag/AgCl. Nevertheless, the registered value is much lower than Au's potential in the same environment (Figure S5). As the ITO glass+Nafion® presents a higher OCP, the difference can be solely attributed to the defects present on the Au coating, which expose the underlying NiCo to the electrolyte. The addition of BSA protein into the PBS solution led to a decrease in the OCP in both cases by inhibiting the cathodic reactions and covering the active sites on the heterogeneous surface by chemisorbed bonds [39, 46].

Fig. 6b shows representative PDP curves of NiCo and NiCo/Au-MP in PBS and PBS+1 $g.L^{-1}$ BSA solutions at 25 °C and aerated conditions, together with the curves corresponding to ITO glass and ITO glass+Nafion® in PBS solution. The corrosion potential ($E_{corr}$) and the corrosion current density ($i_{corr}$), extrapolated using the Tafel equations, and together with the passive current density ($i_{pass}$), are reported in Table 1.

The $E_{corr}$ values of the different analysed specimens, extrapolated from the PDP curves, confirmed the galvanic series observed in the OCP measurements. Prior discussing on the current density evolution of the different PDP curves, it is fair to point out that, considering the different materials that compose the samples, under anodic polarization in the investigated range of potential, on the surface of the ITO glass (stable conductive oxide in a wide potential range), the Nafion® (conductive polymer, stable in a wide potential range) and the Au (inert metal in a wide potential range and environments), the anodic reactions can only concern the oxidation of the components present in the electrolyte, such as phosphate species ($HPO_4^{2-}$ and $H_2PO_4^-$) [38]. Based on this statement, the anodic branches of the PDP curves of both ITO glass and ITO glass+Nafion® show a progressive increase of the anodic current by increasing the potential due to the oxidation of the components in the solution. The higher the driving force, the higher the oxidation rate of the species in the solution and hence the measured current.

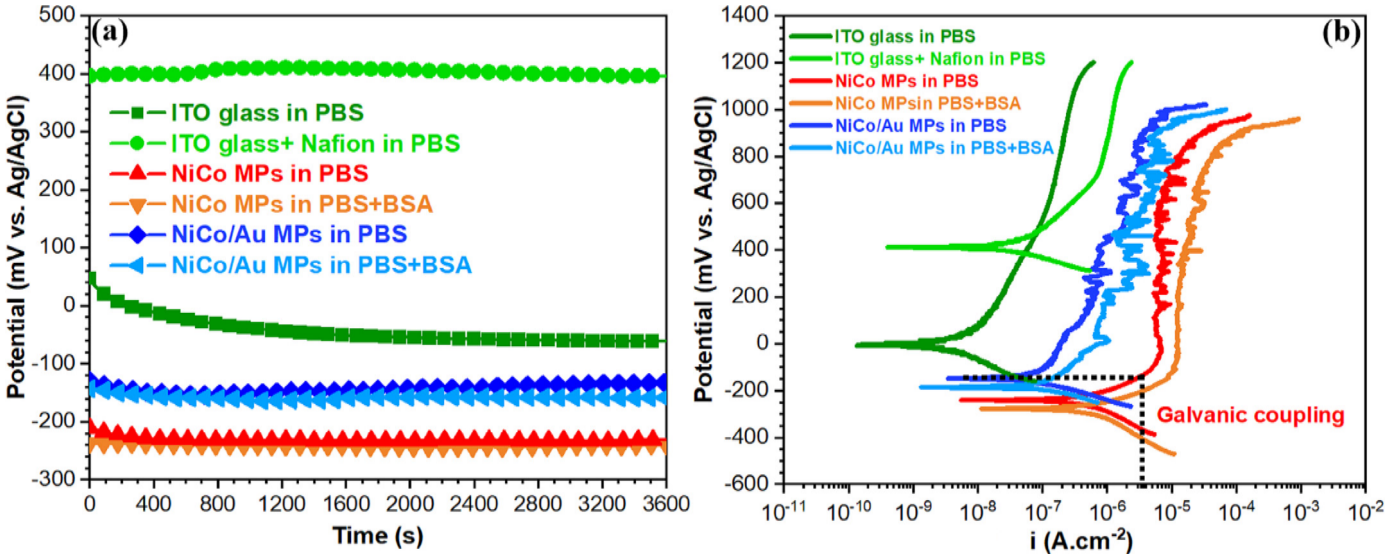


**Fig. 6.** (a) OCP and (b) PDP curves of NiCo and NiCo/Au-MPs coated with Nafion® on ITO glass in PBS and PBS+BSA solutions at 25 °C and pH 7.4.

**Table 1.**
$i_{corr}$, $E_{corr}$ and $i_{pass}$ data obtained from PDP curves in Fig. 6b.

| Samples | $i_{corr}$ (A.cm$^{-2}$) | $E_{corr}$ (mV vs. Ag/AgCl) | $i_{pass}$ (A.cm$^{-2}$) |
|---|---|---|---|
| ITO glass in PBS | $1 \pm 0.2 \times 10^{-8}$ | −10±2 | |
| ITO glass+Nafion® in PBS | $6 \pm 0.5 \times 10^{-8}$ | 415±50 | |
| NiCo MPs in PBS | $5 \pm 0.5 \times 10^{-7}$ | −240±15 | $7 \pm 0.3 \times 10^{-6}$ |
| NiCo MPs in PBS+BSA | $7 \pm 1 \times 10^{-7}$ | −285±25 | $1.2 \pm 0.2 \times 10^{-5}$ |
| NiCo/Au MPs in PBS | $6 \pm 0.6 \times 10^{-8}$ | −140±20 | $4 \pm 0.5 \times 10^{-7}$ |
| NiCo/Au MPs in PBS+BSA | $9 \pm 0.8 \times 10^{-8}$ | −180±20 | $9 \pm 0.5 \times 10^{-7}$ |

The optimization of the sample production method containing the two types of MPs substantiates the fact that the metallic area exposed to the electrolyte is essentially the same. By considering that up to 400 mV vs. Ag/AgCl ($E_{corr}$ of the ITO glass+Nafion®) the Nafion® is under cathodic polarization, the anodic currents of the samples containing MPs are attributable only to the reactions that take place on the exposed metallic surfaces. Due to the active-passive behavior of the NiCo alloy, the anodic reactions can be mainly attributed to its oxidation under anodic polarization. The anodic branch of the PDP curves of the sample containing the NiCo-MPs showed a passive behavior of up to around 200 mV vs. Ag/AgCl. Nevertheless, above a value of around 200 mV vs. Ag/AgCl, fluctuations of the anodic current suggest triggering of metastable pits [69]. Moreover, the NiCo-MPs anodic current was higher in comparison to all other types of samples due to the contribution of the metal oxidation. The anodic current measured on the specimens containing NiCo/Au-MPs is the sum of two distinguished phenomena: the oxidation of the species present in the electrolyte on the surface of the Au coating, and the oxidation of the NiCo alloy through the pores or defects of the Au coating [69, 70], similar to the measured $E_{corr}$ being a mixed potential of the Au and the uncovered NiCo substrate through the coating defects. In order to confirm this hypothesis, PDP curves were obtained, under the same conditions, on a pure Au sheet and on a 1 mm thick electroformed NiCo alloy with a chemical composition similar to that of the MPs (Figure S5). The obtained curves have a similar form to those obtained on the MPs, but the $E_{corr}$ of the pure Au is much higher than that of the NiCo/Au-MPs, confirming the hypothesis of measuring a mixed potential. Considering that the area of the Au coating largely exceeds the exposed area of NiCo substrate, it is fair to assume that in free corrosion conditions, the galvanic potential ($E_{galvanic(NiCo)/(Au)}$) due to the coupling between different materials is near to the $E_{corr}$ of the NiCo/Au-MPs sample revealed by the PDP measurements. Therefore, the exposed NiCo substrate will be oxidized with a corrosion rate that corresponds to the anodic current of the NiCo-MPs at the same potential (vertical dashed line in Fig. 6b), and higher than the corrosion current density of the NiCo-MPs. Nevertheless, relying only on the PDP measurements, it is difficult to establish if this relatively small over-potential ($E_{galvanic(NiCo)/(Au)} \approx E_{corr\ NiCo/Au} - E_{corr\ NiCo} \approx 100$ mV) caused by the galvanic coupling is high enough to trigger the localized corrosion of the NiCo alloy and a significant release of Ni and Co ions to the electrolyte. The fluctuations of the anodic current above 200 mV vs. Ag/AgCl for the NiCo/Au-MPs also indicates the formation of metastable pits [70].

The addition of BSA in the PBS electrolyte leads to a decrease in the $E_{corr}$ and an increase of both $i_{corr}$ and anodic current density of both samples containing MPs, suggesting an increase in the aggressiveness of the electrolyte. The BSA, known as the strongest metal binder amongst human blood proteins with a high concentration in synovial fluid [49], is a strong promoter of metal ions release for a wide range of biomedical alloys [38, 71-73]. Although it takes time to express its aggressiveness, as it interacts slowly following different mechanisms (adsorption, protein-metal binding, metal ion detachment [49]), in our experiments, the effect on the decrease of the corrosion resistance is already demonstrated after 1 hour of immersion by the PDPs. The shape of the PDP curves showed a similar effect on the addition of BSA proteins for both types of MPs, but the difference in the anodic currents was much more evident with the NiCo-MPs with respect to the NiCo/Au-MPs. Assuming that the Au is essentially inert to the presence of BSA in the solution, with the exception of the possible adsorption phenomena, the higher the NiCo surface exposed to the electrolyte, the higher the oxidation phenomena and hence the anodic current measured during the potential scan.

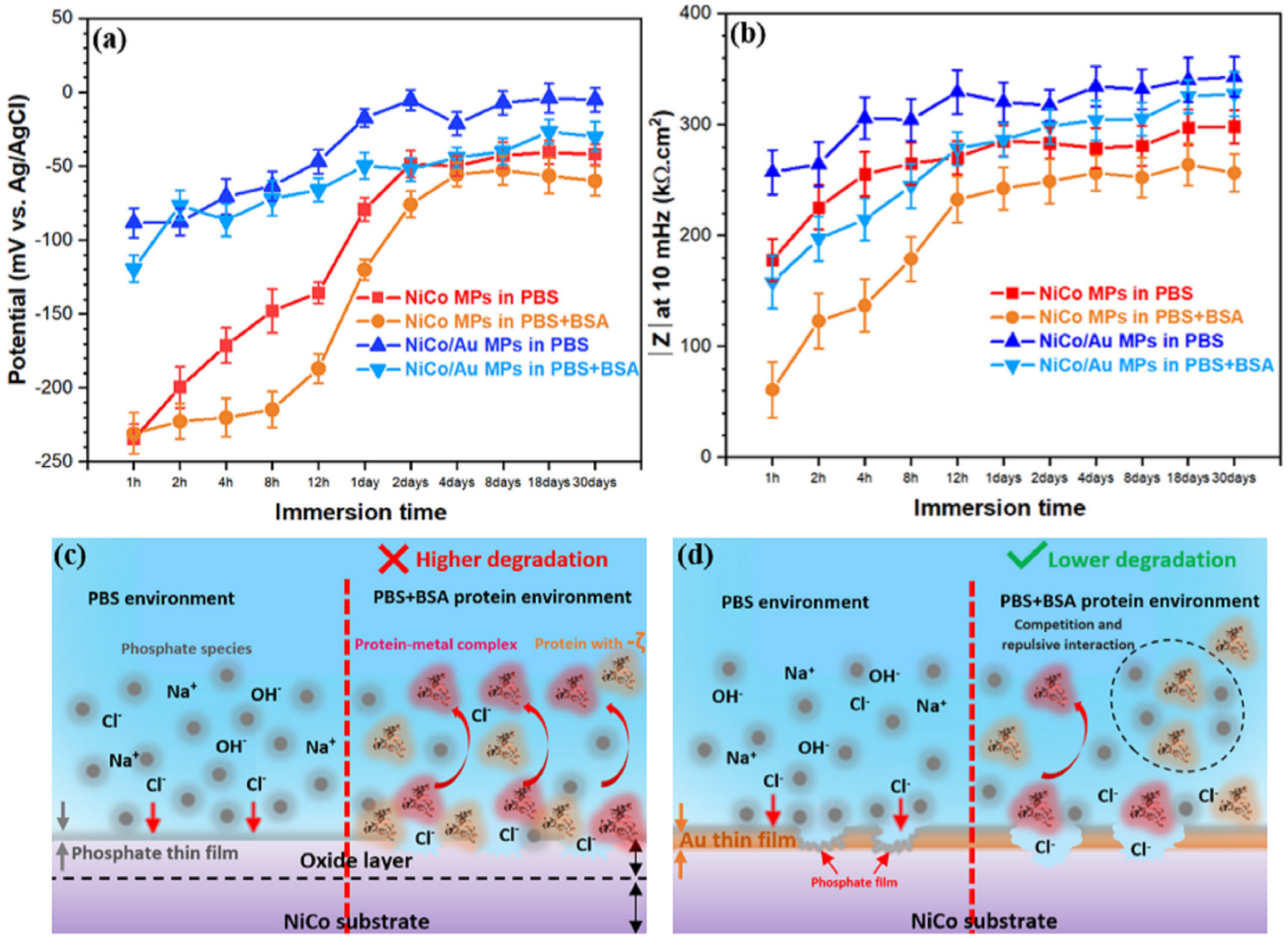


**Fig. 7.** (a) OCP and (b) |Z| at 10 mHz during long-term immersion tests of NiCo and NiCo/Au-MPs immersed in PBS and PBS+BSA at 25 °C and pH 7.4, Schematic presentation of phosphate species adsorption and BSA protein interaction and its role on metal ion releasing on (c) NiCo and (d) NiCo/Au-MPs in the different environments.

As a consequence, the SKPFM analyses and the PDP measurements revealed the galvanic coupling between the Au and the uncovered areas of the NiCo substrate through the Au layer defects. However, it does not give an indication of the long-term corrosion in simulated body fluids and the metal ions release. To this aim, long-term immersion tests were considered necessary and will be discussed in the next section.

### 3.3. Long-term immersion tests

#### 3.3.1. EIS measurements

As reported in the experimental section, ITO glass with a Nafion® coating containing either NiCo or NiCo/Au-MPs were immersed in either PBS or PBS+BSA solutions for 30 days, then OCP and EIS measurements were performed at regular intervals. Bode magnitude and phase diagrams of the EIS measurements can be found in Figure S6. From the Bode plots, it is clear that the NiCo-MPs present a lower impedance than the NiCo/Au-MPs immediately after immersion and that the addition of BSA in the electrolyte lowers the impedance of both systems. However, by increasing the immersion time, an increase of the impedance magnitude was observed in all tested systems, along with a flattening of the phase diagram, indicating a transition from a single time constant system to a two-time constant system. This increase was much more evident in BSA-containing electrolytes, which presented the lowest values immediately after immersion. Assuming that Nafion® has a similar effect on all studied systems, the main contribution to the charge transfer resistance corresponds to the metal elements (Ni, Co and Au). For this reason, the impedance modulus at 10 mHz was used to compare all specimens' performances. The results together with the OCP values monitored during the 30 days of immersion are reported in Fig. 7a and b.

From Fig. 7a, it is evident that all samples showed a marked increase of the OCP during the first two days of immersion and then reach a virtual steady state. The NiCo/Au-MPs consistently showed higher potential values in both environments due to the presence of an Au coated layer. The increase of the OCP was, however, more evident on the NiCo-MPs, so that all samples reached values of the same order of magnitude after long immersion times, always maintaining the order NiCo/Au in PBS>NiCo/Au in PBS+BSA>NiCo in PBS>NiCo in PBS+BSA. The same behavior was observed by the impedance modulus at 10 mHz (Fig. 7b). In addition, an increase was shown during the first two days followed by a stabilization of up to 30 days. The presence of the Au layer increased the impedance values, while the addition of the BSA protein led to lower values. This was due to the formation of a thin film of phosphates on the MPs' surface after the immersion in the electrolyte [39], which offered a barrier protection for the metal ion release. After longer immersion times, the stability of the phosphates film increased, and both OCP and |Z| values reached a steady state. The BSA protein was also adsorbed on the specimens' surface as it ex-

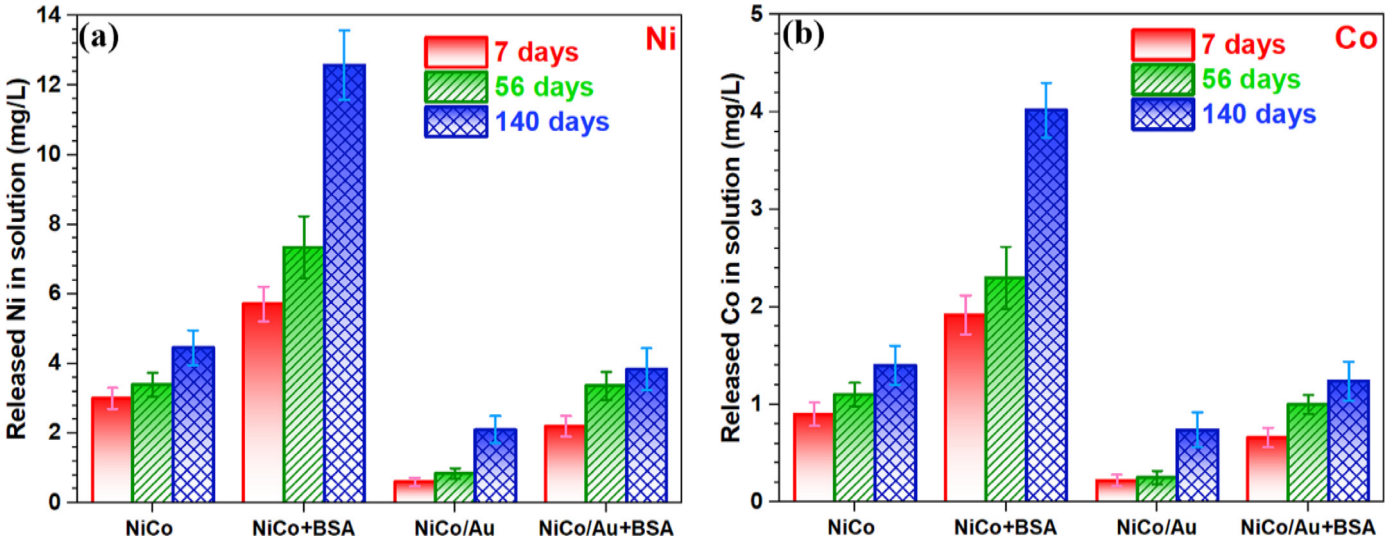


**Fig. 8.** Total amounts of (a) Ni and (b) Co released from NiCo and NiCo/Au-MPs after immersion for 7, 56 and 140 days in PBS and PBS+BSA at 25 °C and with a pH 7.4.

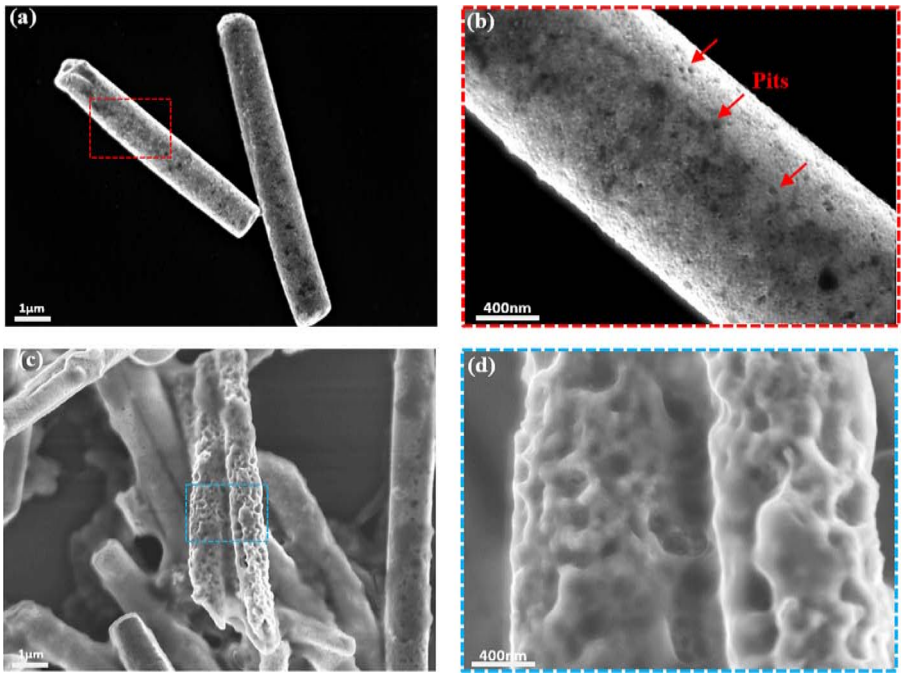


**Fig. 9.** Low and high magnification FE-SEM images of NiCo-MPs after immersion in (a and b) PBS and (c and d) PBS+BSA solution for 56 days.

hibited a negative ζ potential at pH 7.4 [39]. The BSA molecules competed with the phosphate species to form the adsorbed film, lowering both the OCP and |Z| values. The adsorbed layers provided a shielding effect to the aggressive $Cl^-$ attack and the corrosion of the NiCo/Au-MPs due to galvanic coupling. However, the BSA proteins can exhibit detrimental effects towards the NiCo passive film. Indeed, BSA interacts with the metal atoms in the oxide layer and, if the metal-protein bonds are stronger than the metal-oxygen bonds, leads to the detachment of protein-metal complexes, increasing the metal ions release and hence the degradation phenomena [49]. The process is schematically represented in Fig. 7c and d.

### *3.3.2. Metal ions release and morphological evaluation of the degradation*

To clarify if the adsorbed phosphates layer slows down the metal ion release due to the presence of Cl– or galvanic coupling between the NiCo substrate and the Au coating, and to confirm that the presence of BSA enhances the corrosion of the MPs, NiCo and NiCo/Au-MPs non-supported on Nafion®, were immersed in PBS and PBS+BSA solutions for a total time of 140 days. Both solutions and immersed MPs were characterized at different intervals to evaluate the degradation.

No significant changes on the pH of the solutions have been noticed. The Ni and Co ions concentration in the two solutions after 7, 56, and 140 days of immersion, as measured by ICP-AES, are reported in Figs. 8a and b. The results demonstrated that higher amounts of both Ni and Co were released from the NiCo-MPs with respect to the NiCo/Au-MPs, proving the protection offered by the Au, despite the defects. The Ni release was around three times higher in comparison to the Co, respecting the alloy chemical composition. Finally, the addition of BSA protein increased the electrolyte's aggressiveness due to the protein-metal bonding effect, leading to an increase of around 200% and 80% (after 140 days of immersion) in the Ni ion release for the NiCo and NiCo/Au-MPs, respectively. This difference is mainly due to the different NiCo

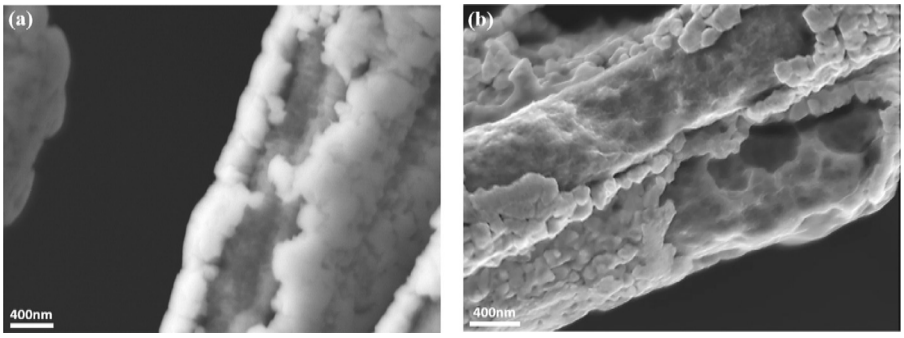


**Fig. 10.** FE-SEM images of NiCo/Au-MPs after immersion in (a) PBS and (b) PBS+BSA solutions for 56 days.

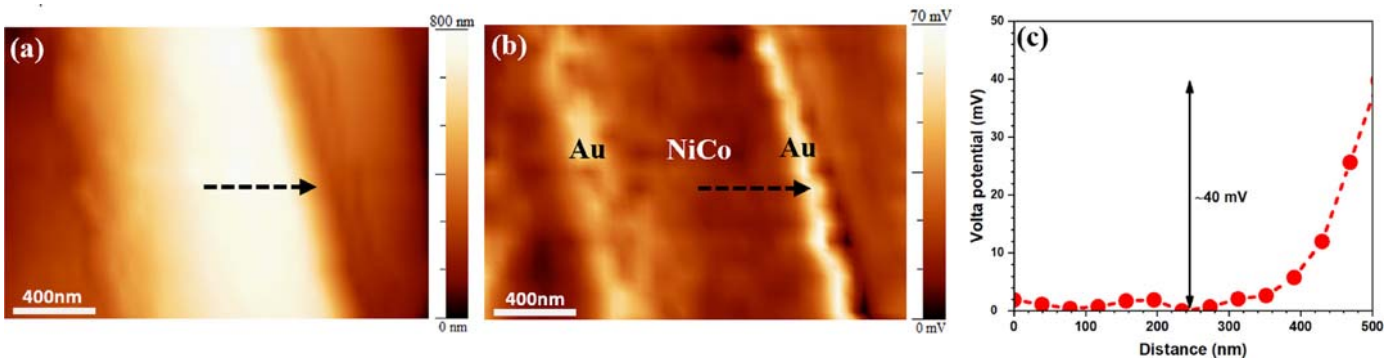


**Fig. 11.** (a) AFM and (b) SKPFM images of NiCo/Au-MPs after immersion in PBS+BSA solution for 56 days, (c) surface Volta potential line profile in (b).

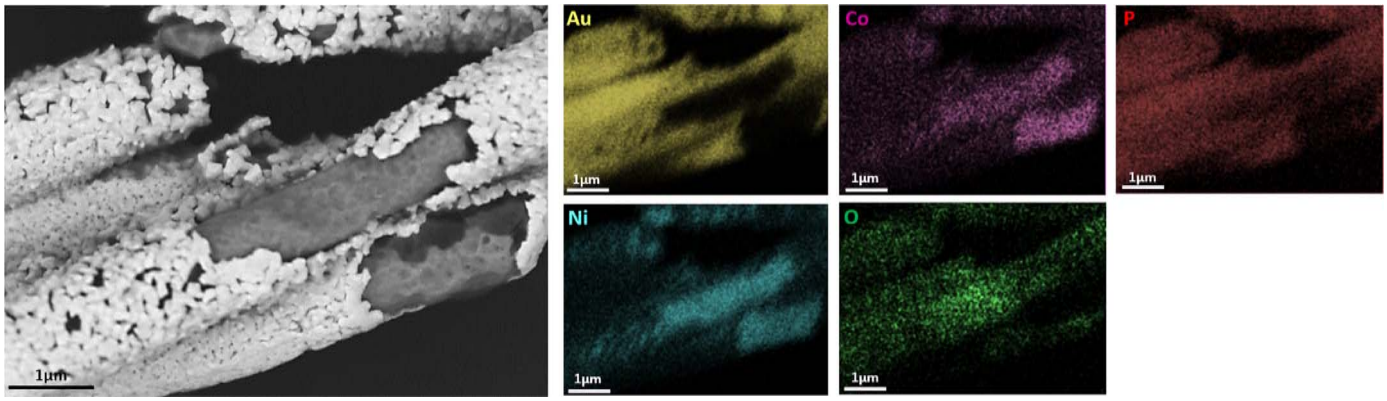


**Fig. 12.** SEM micrograph and EDXS elemental maps of NiCo/Au-MPs after immersion in PBS+BSA solution for 56 days.

exposed areas in the two cases and the fact that the detrimental effect of BSA concerns only the NiCo. This exacerbated metal ion release and its effect on the magnetic manoeuvrability of the NiCo-MPs was verified by magnetic manipulation of a swarm of these structures (see video S1). The videos provided show clearly that the uncorroded NiCo-MPs are quickly attracted to the magnet, while the corroded (after 140 days) hardly move from their initial position, thus clearly indicating a degradation of the magnetic properties. The degradation after 140 days was so massive that made unviable the assessment of the degradation mechanism on the structures. For this reason, we chose 56 days as the time period that would enable the comparison amongst the different specimens and environments to highlight the differences in the degradation mechanisms.

FE-SEM images of both types of MPs after 56 days of immersion in both PBS and PBS+BSA solutions are reported in Figs. 9 and 10. The surface of the NiCo-MPs immersed in PBS solution was relatively uniform and was covered by a thick oxide-phosphates layer, where small dimension pits (red arrows Fig. 9b) could be attributed to the $Cl^-$attack. The corrosion attack in the presence of BSA was much more intense and led to a severely grooved surface (Fig. 9c and d). This is due to the protein-metal bonding and the detachment of the protein-metal complexes [49, 74]. The immersion of NiCo/Au-MPs in PBS solution for 56 days led to an intense corrosive attack on the NiCo through the Au layer defects (Fig. 10a), proving the galvanic coupling. The dissolution of the NiCo through the defects was striking compared to that of NiCo-MPs immersed in the same solution (Fig. 9a and b). The presence of BSA protein intensified the corrosion attack and the uncovered NiCo surface appeared highly degraded, with the same morphology observed in the NiCo-MPs immersed in the same environment. The effect of the BSA protein also had an indirect impact on the morphology of the Au coating. The more intensive dissolution of the NiCo, not only as a result of the defects but also from the Au grain-boundaries, makes the Au layer appear as not continuous but as isolated grains (Fig. 10b).

However, the dissolution of NiCo through the Au defects was not as severe as expected from the galvanic coupling, observed by

the PDP curves and SKPFM measurements. After long-immersion times, the formation of a phosphates film, as observed in the increase of both OCP and |Z|, could attenuate this difference. To confirm this hypothesis, AFM and SKPFM maps from a defective area of NiCo/Au-MP immersed for 56 days in PBS+BSA solution were obtained and reported in Fig. 11, together with the Volta potential line profile. In the SKPFM map, the Volta potential difference between the NiCo and the Au is clearly visible (Fig. 11b), but as demonstrated by the line profile, this difference is around 40 mV, which is much lower than that observed before immersion (~120 mV, Fig. 5c). The SKPFM analyses proved that during long-immersion times, the Volta potential difference between NiCo and Au, a driving force for the galvanic coupling, is significantly decreased due to the formation of the phosphates-oxides film [71] on the whole surface, as presented in Fig. 12. Indeed, from the EDXS maps the presence of P over the whole MPs surface is confirmed.

## 4. Conclusions

In this work, the degradation of NiCo-micropillars (NiCo-MPs), both uncoated and Au-coated, during immersion in phosphate-buffered solution containing bovine serum albumin was studied, for the first time, using a combination of electrochemical and surface analyses techniques. The resultant NiCo-MPs present a smooth surface and a uniform chemical composition. However, the Au coating on the NiCo/Au-MPs did not uniformly cover the MPs surface, presenting uncovered regions and micro- and nano-sized defects. SKPFM and potentiodynamic polarization measurements revealed the galvanic coupling between the Au and the uncovered areas of the NiCo substrate as a result of the Au layer defects, which could increase the dissolution rate of the NiCo. Conversely, long-term EIS measurements showed that a phosphate-based layer was formed on the MPs' surface, which became more stable after longer immersion times, providing a shielding effect from the aggressive $Cl^-$ attack and the corrosion of the NiCo/Au-MPs due to galvanic coupling. The formation of the phosphates film after long immersion times decreased the Volta potential difference between the Au layer and the NiCo substrate exposed by the defects as demonstrated by the SKPFM measurements. Metal ions release measurements performed for 140 days demonstrated that, despite its defects, the Au coating provided certain protection, lowering the Ni and Co release in the electrolyte of around 60% and 50%, respectively.

The presence of BSA increased the aggressiveness of the electrolyte, as demonstrated by all electrochemical measurements. The BSA molecules competed with the phosphate species to form the adsorbed film on the MPs' surface and increased the corrosion rate due to the protein-metal bonding and the detachment of the protein-metal complexes. This was confirmed by the metal ions' release measurements and the observation of the corrosion attack morphology on the different pillars after long-term immersion tests. BSA's presence led to an increase in the Ni release of about 200% and 80% after 140 days of immersion for the NiCo and NiCo/Au-MPs, respectively. The NiCo corroded surface, in BSA's presence, was much rougher in both cases when compared to immersion in only PBS solution. In addition, the Au coating offered certain protection, despite the defects, due to the fact that the BSA detrimental effect only had an impact on the NiCo, and the exposed area through the defects was significantly lower in comparison with the non-coated NiCo-MPs.

## Credit author statement

**Ehsan Rahimi**: methodology, investigation, writing original draft

**Ruben Offoiach**: methodology, investigation, writing - review and editing

**Siyu Deng**: investigation

**Xiangzhong Chen:** investigation

**Salvador Pané**: writing - review and editing, resources, funding acquisition, supervision

**Lorenzo Fedrizzi:** writing - review and editing, resources, supervision

**Maria Lekka:** methodology, writing –review and editing, resources, funding acquisition, supervision, project administration

## Data availability statement

The raw/processed data required to reproduce these findings cannot be shared at this time as the data also forms part of an ongoing study.

## Declaration of Competing Interest

None.

## Acknowledgments

This project has received funding from the European Union's Horizon 2020 research and innovation program under the Marie Sklodowska-Curie grant agreements no 764977.

## Supplementary materials

Supplementary material associated with this article can be found, in the online version, at doi:10.1016/j.apmt.2021.101135.

## References

[1] J.G.S. Moo, C.C. Mayorga-Martinez, H. Wang, B. Khezri, W.Z. Teo, M. Pumera, Nano/microrobots meet electrochemistry, Adv. Funct. Mater. 27 (12) (2017) 1604759.
[2] D. Xu, Y. Wang, C. Liang, Y. You, S. Sanchez, X. Ma, Self-propelled micro/nanomotors for on-demand biomedical cargo transportation, Small (2019) 1902464.
[3] J. Katuri, X. Ma, M.M. Stanton, S. Sánchez, Designing micro-and nanoswimmers for specific applications, Acc. Chem. Res. 50 (1) (2017) 2–11.
[4] W. Gao, J. Wang, Synthetic micro/nanomotors in drug delivery, Nanoscale 6 (18) (2014) 10486–10494.
[5] F. Alouges, A. DeSimone, A. Lefebvre, Optimal strokes for low Reynolds number swimmers: an example, J. Nonlinear Sci. 18 (3) (2008) 277–302.
[6] P. Fischer, A. Ghosh, Magnetically actuated propulsion at low Reynolds numbers: towards nanoscale control, Nanoscale 3 (2) (2011) 557–563.
[7] M. You, C. Chen, L. Xu, F. Mou, J. Guan, Intelligent micro/nanomotors with Taxis, Acc. Chem. Res. 51 (12) (2018) 3006–3014.
[8] M. Guix, C.C. Mayorga-Martinez, A. Merkoçi, Nano/micromotors in (bio) chemical science applications, Chem. Rev. 114 (12) (2014) 6285–6322.
[9] J. Li, B.E.-F. de Ávila, W. Gao, L. Zhang, J. Wang, Micro/nanorobots for biomedicine: delivery, surgery, sensing, and detoxification, Sci. Robot. 2 (4) (2017).
[10] J. Li, I. Rozen, J. Wang, Rocket science at the nanoscale, ACS Nano 10 (6) (2016) 5619–5634.
[11] X.Z. Chen, B. Jang, D. Ahmed, C. Hu, C. De Marco, M. Hoop, F. Mushtaq, B.J. Nelson, S. Pané, Small-scale machines driven by external power sources, Adv. Mater. 30 (15) (2018) 1705061.
[12] H. Wang, M. Pumera, Fabrication of micro/nanoscale motors, Chem. Rev. 115 (16) (2015) 8704–8735.
[13] X.-Z. Chen, M. Hoop, F. Mushtaq, E. Siringil, C. Hu, B.J. Nelson, S. Pané, Recent developments in magnetically driven micro-and nanorobots, Appl. Mater. Today 9 (2017) 37–48.
[14] S. Pané, J. Puigmartí-Luis, C. Bergeles, X.Z. Chen, E. Pellicer, J. Sort, V. Počepcová, A. Ferreira, B.J. Nelson, Imaging Technologies for Biomedical Micro-and Nanoswimmers, Adv. Mater. Technol. 4 (4) (2019) 1800575.
[15] C.C. Alcântara, S. Kim, S. Lee, B. Jang, P. Thakolkaran, J.Y. Kim, H. Choi, B.J. Nelson, S. Pané, 3D Fabrication of fully iron magnetic microrobots, Small 15 (16) (2019) 1805006.
[16] C. Hu, F. Aeschlimann, G. Chatzipirpiridis, J. Pokki, X. Chen, J. Puigmarti-Luis, B.J. Nelson, S. Pané, Spatiotemporally controlled electrodeposition of magnetically driven micromachines based on the inverse opal architecture, Electrochem. Commun. 81 (2017) 97–101.

[17] F. Mushtaq, H. Torlakcik, M. Hoop, B. Jang, F. Carlson, T. Grunow, N. Läubli, A. Ferreira, X.Z. Chen, B.J. Nelson, Motile piezoelectric nanoeels for targeted drug delivery, Adv. Funct. Mater. 29 (12) (2019) 1808135.
[18] S. Schuerle, I.A. Vizcarra, J. Moeller, M.S. Sakar, B. Özkale, A.M. Lindo, F. Mushtaq, I. Schoen, S. Pané, V. Vogel, Robotically controlled microprey to resolve initial attack modes preceding phagocytosis, Sci. Robot. 2 (2017) eaah6094.
[19] J. Wang, Template electrodeposition of catalytic nanomotors, Faraday Discuss. 164 (2013) 9–18.
[20] F. Qiu, B.J. Nelson, Magnetic helical micro- and nanorobots: toward their biomedical applications, Engineering 1 (1) (2015) 021–026.
[21] M. Koleoso, X. Feng, Y. Xue, Q. Li, T. Munshi, X. Chen, Micro/nanoscale magnetic robots for biomedical applications, Mater. Today Bio. 8 (2020) 100085.
[22] M. Safi, M. Yan, M.-.A. Guedeau-Boudeville, H. Conjeaud, V. Garnier-Thibaud, N. Boggetto, A. Baeza-Squiban, F. Niedergang, D. Averbeck, J.-.F. Berret, Interactions between magnetic nanowires and living cells: uptake, toxicity, and degradation, ACS Nano 5 (7) (2011) 5354–5364.
[23] J. Kolosnjaj-Tabi, Y. Javed, L. Lartigue, J. Volatron, D. Elgrabli, I. Marangon, G. Pugliese, B. Caron, A. Figuerola, N. Luciani, The one year fate of iron oxide coated gold nanoparticles in mice, ACS Nano 9 (8) (2015) 7925–7939.
[24] D. Ling, T. Hyeon, Chemical design of biocompatible iron oxide nanoparticles for medical applications, Small 9 (9–10) (2013) 1450–1466.
[25] X. He, P. Hahn, J. Iacovelli, R. Wong, C. King, R. Bhisitkul, M. Massaro-Giordano, J.L. Dunaief, Iron homeostasis and toxicity in retinal degeneration, Prog. Retin. Eye Res. 26 (6) (2007) 649–673.
[26] Y. Okazaki, E. Gotoh, Comparison of metal release from various metallic biomaterials in vitro, Biomaterials 26 (1) (2005) 11–21.
[27] F. Mou, C. Chen, H. Ma, Y. Yin, Q. Wu, J. Guan, Self-propelled micromotors driven by the magnesium–water reaction and their hemolytic properties, Angew. Chem. Int. Ed. 52 (28) (2013) 7208–7212.
[28] Y. Yoshizumi, K. Okubo, M. Yokokawa, H. Suzuki, Programmed transport and release of cells by self-propelled micromotors, Langmuir 32 (37) (2016) 9381–9388.
[29] W. Gao, A. Pei, J. Wang, Water-driven micromotors, ACS Nano 6 (9) (2012) 8432–8438.
[30] H.H. Jeong, M. Alarcón-Correa, A.G. Mark, K. Son, T.C. Lee, P. Fischer, Corrosion-protected hybrid nanoparticles, Adv. Sci. 4 (12) (2017) 1700234.
[31] I. Spajić, E. Rahimi, M. Lekka, R. Offoiach, L. Fedrizzi, I. Milošev, Al2O3 and HfO2 atomic layers deposited in single and multilayer configurations on titanium and on stainless steel for biomedical applications, J. Electrochem. Soc. 168 (7) (2021) 071510.
[32] S.K. Srivastava, B. Ghosh, 5 - Metallic biomaterials for dental implant systems, in: P. Balakrishnan, M S S., S. Thomas (Eds.), Fundamental Biomaterials: Metals, Woodhead Publishing, 2018, pp. 111–137.
[33] G. Zhao, B. Khezri, S. Sanchez, O.G. Schmidt, R.D. Webster, M. Pumera, Corrosion of self-propelled catalytic microengines, Chem. Commun. 49 (80) (2013) 9125–9127.
[34] T. Maric, M.Z.M. Nasir, M. Budanovic, O. Alduhaish, R.D. Webster, M. Pumera, Corrosion of light powered Pt/TiO2 microrobots, Appl. Mater. Today 20 (2020) 100659.
[35] F. Wong, A. Sen, Progress toward light-harvesting self-electrophoretic motors: highly efficient bimetallic nanomotors and micropumps in halogen media, ACS Nano 10 (7) (2016) 7172–7179.
[36] J. Pokki, O. Ergeneman, G. Chatzipirpiridis, T. Lühmann, J. Sort, E. Pellicer, S.A. Pot, B.M. Spiess, S. Pané, B.J. Nelson, Protective coatings for intraocular wirelessly controlled microrobots for implantation: corrosion, cell culture, and in vivo animal tests, J. Biomed. Mater. Res. Part B 105 (4) (2017) 836–845.
[37] D. Mei, S.V. Lamaka, X. Lu, M.L. Zheludkevich, Selecting medium for corrosion testing of bioabsorbable magnesium and other metals – A critical review, Corros. Sci. 171 (2020) 108722.
[38] I. Milošev, CoCrMo alloy for biomedical applications, in: Biomedical Applications, Springer, 2012, pp. 1–72.
[39] E. Rahimi, R. Offoiach, K. Baert, H. Terryn, M. Lekka, L. Fedrizzi, Role of phosphate, calcium species and hydrogen peroxide on albumin protein adsorption on surface oxide of Ti6Al4V alloy, Materialia 15 (2021) 100988.
[40] C.V. Vidal, A.I. Muñoz, Study of the adsorption process of bovine serum albumin on passivated surfaces of CoCrMo biomedical alloy, Electrochim. Acta 55 (28) (2010) 8445–8452.
[41] Y. Yan, H. Yang, Y. Su, L. Qiao, Albumin adsorption on CoCrMo alloy surfaces, Sci. Rep. 5 (1) (2015) 1–10.
[42] C.V. Vidal, A.I. Muñoz, Effect of physico-chemical properties of simulated body fluids on the electrochemical behaviour of CoCrMo alloy, Electrochim. Acta 56 (24) (2011) 8239–8248.
[43] S. Karimi, A. Alfantazi, Electrochemical corrosion behavior of orthopedic biomaterials in presence of human serum albumin, J. Electrochem. Soc. 160 (6) (2013) C206.
[44] Y.S. Hedberg, M. Žnidaršič, G. Herting, I. Milošev, I. Odnevall Wallinder, Mechanistic insight on the combined effect of albumin and hydrogen peroxide on surface oxide composition and extent of metal release from Ti6Al4V, J. Biomed. Mater. Res. Part B 107 (3) (2019) 858–867.
[45] E. Rahimi, R. Offoiach, S. Hosseinpour, A. Davoodi, K. Baert, A. Lutz, H. Terryn, M. Lekka, L. Fedrizzi, Effect of hydrogen peroxide on bovine serum albumin adsorption on Ti6Al4V alloy: a scanning Kelvin probe force microscopy study, Appl. Surf. Sci. 563 (2021) 150364.
[46] S. Karimi, T. Nickchi, A. Alfantazi, Effects of bovine serum albumin on the corrosion behaviour of AISI 316 L, Co–28Cr–6Mo, and Ti–6Al–4 V alloys in phosphate buffered saline solutions, Corros. Sci. 53 (10) (2011) 3262–3272.
[47] Y. Hedberg, X. Wang, J. Hedberg, M. Lundin, E. Blomberg, I.O. Wallinder, Surface-protein interactions on different stainless steel grades: effects of protein adsorption, surface changes and metal release, J. Mater. Sci. 24 (4) (2013) 1015–1033.
[48] W. Xu, F. Yu, L. Yang, B. Zhang, B. Hou, Y. Li, Accelerated corrosion of 316 L stainless steel in simulated body fluids in the presence of H2O2 and albumin, Mater. Sci. Eng. 92 (2018) 11–19.
[49] Y.S. Hedberg, Role of proteins in the degradation of relatively inert alloys in the human body, npj Mater. Degrad. 2 (1) (2018) 1–5.
[50] X. Xu, L. Xiao, Y. Jia, Z. Wu, F. Wang, Y. Wang, N.O. Haugen, H. Huang, Pyro–catalytic hydrogen evolution by Ba 0.7 Sr 0.3 TiO 3 nanoparticles: harvesting cold–hot alternation energy near room-temperature, Energy Environ. Sci. 11 (8) (2018) 2198–2207.
[51] X. Yang, Q. Yang, J. Xu, C.-.S. Lee, Bimetallic PtPd nanoparticles on Nafion–graphene film as catalyst for ethanol electro-oxidation, J. Mater. Chem. 22 (16) (2012) 8057–8062.
[52] H. Park, W. Choi, Photocatalytic reactivities of nafion-coated TiO2 for the degradation of charged organic compounds under UV or visible light, J. Phys. Chem. B 109 (23) (2005) 11667–11674.
[53] J. Hong, H. Ghourchian, A.A. Moosavi–Movahedi, Direct electron transfer of redox proteins on a Nafion-cysteine modified gold electrode, Electrochem. Commun. 8 (10) (2006) 1572–1576.
[54] S.A. Bhakta, E. Evans, T.E. Benavidez, C.D. Garcia, Protein adsorption onto nanomaterials for the development of biosensors and analytical devices: a review, Anal. Chim. Acta 872 (2015) 7–25.
[55] X. Zhao, Y. Fu, J. Wang, Y. Xu, J.-.H. Tian, R. Yang, Ni-doped CoFe2O4 hollow nanospheres as efficient Bi-functional catalysts, Electrochim. Acta 201 (2016) 172–178.
[56] G. Ou, F. Wu, K. Huang, N. Hussain, D. Zu, H. Wei, B. Ge, H. Yao, L. Liu, H. Li, Boosting the electrocatalytic water oxidation performance of CoFe2O4 nanoparticles by surface defect engineering, ACS Appl. Mater. Interface. 11 (4) (2019) 3978–3983.
[57] C.A. Schneider, W.S. Rasband, K.W. Eliceiri, NIH Image to ImageJ: 25 years of image analysis, Nat. Methods 9 (7) (2012) 671–675.
[58] S. Karimi, T. Nickchi, A.M. Alfantazi, Long-term corrosion investigation of AISI 316 L, Co–28Cr–6Mo, and Ti–6Al–4 V alloys in simulated body solutions, Appl. Surf. Sci. 258 (16) (2012) 6087–6096.
[59] C. Ma, S. Wang, F. Walsh, Electrodeposition of nanocrystalline nickel–cobalt binary alloy coatings: a review, Trans. IMF 93 (2) (2015) 104–112.
[60] E. Rahimi, A. Rafsanjani-Abbasi, A. Imani, A. Davoodi, TiO2/Cu2O coupled oxide films in Cl– ion containing solution: volta potential and electronic properties characterization by scanning probe microscopy, Mater. Chem. Phys. 212 (2018) 403–407.
[61] M. Rohwerder, F. Turcu, High-resolution Kelvin probe microscopy in corrosion science: scanning Kelvin probe force microscopy (SKPFM) versus classical scanning Kelvin probe (SKP), Electrochim. Acta 53 (2) (2007) 290–299.
[62] P. Schmutz, G. Frankel, Corrosion study of AA2024-T3 by scanning kelvin probe force microscopy and in situ atomic force microscopy scratching, J Electrochem. Soc. 145 (7) (1998) 2295–2306.
[63] C. Barth, A.S. Foster, C.R. Henry, A.L. Shluger, Recent trends in surface characterization and chemistry with high-resolution scanning force methods, Adv. Mater. 23 (4) (2011) 477–501.
[64] A. Cook, Z. Barrett, S. Lyon, H. McMurray, J. Walton, G. Williams, Calibration of the scanning Kelvin probe force microscope under controlled environmental conditions, Electrochim. Acta 66 (2012) 100–105.
[65] C. Örnek, C. Leygraf, J. Pan, On the Volta potential measured by SKPFM–fundamental and practical aspects with relevance to corrosion science, Corrosion Engineering, Sci. Technol. 54 (3) (2019) 185–198.
[66] E. Rahimi, A. Rafsanjani-Abbasi, A. Imani, S. Hosseinpour, A. Davoodi, Correlation of surface Volta potential with galvanic corrosion initiation sites in solid-state welded Ti-Cu bimetal using AFM-SKPFM, Corros. Sci. 140 (2018) 30–39.
[67] Z. Esfahani, E. Rahimi, M. Sarvghad, A. Rafsanjani-Abbasi, A. Davoodi, Correlation between the histogram and power spectral density analysis of AFM and SKPFM images in an AA7023/AA5083 FSW joint, J. Alloys Compd. 744 (2018) 174–181.
[68] T. Mashio, K. Malek, M. Eikerling, A. Ohma, H. Kanesaka, K. Shinohara, Molecular dynamics study of ionomer and water adsorption at carbon support materials, J. Phys. Chem. C 114 (32) (2010) 13739–13745.
[69] D.A. Shores, Corrosion and metal release rates of Ni substrates under a porous gold coating, Corros. Sci. 50 (2) (2008) 372–383.
[70] G.S. Frankel, T. Li, J.R. Scully, Perspective—Localized corrosion: passive film breakdown vs pit growth stability, J. Electrochem. Soc. 164 (4) (2017) C180.
[71] I. Milošev, The effect of biomolecules on the behaviour of CoCrMo alloy in various simulated physiological solutions, Electrochim. Acta 78 (2012) 259–273.
[72] F. Yu, O. Addison, A.J. Davenport, A synergistic effect of albumin and H2O2 accelerates corrosion of Ti6Al4V, Acta Biomater. 26 (2015) 355–365.
[73] M.H. Wood, C.G. Payagalage, T. Geue, Bovine Serum albumin and fibrinogen adsorption at the 316 L stainless steel/aqueous interface, J. Phys. Chem. B 122 (19) (2018) 5057–5065.
[74] M. Talha, Y. Ma, P. Kumar, Y. Lin, A. Singh, Role of protein adsorption in the bio corrosion of metallic implants–A review, Colloid. Surface. B 176 (2019) 494–506.